Wavelength-Dependent Photolysis of Glyoxal in the 290−420 nm Region

Yunqing Chen and Lei Zhu*

Wadsworth Center, New York State Department of Health, Department of Environmental Health and Toxicology, State University of New York, Albany, New York 12201-0509

Received: November 14, 2002; In Final Form: April 7, 2003

We have studied the gas-phase photolysis of glyoxal, $(CHO)_2$, at 10 nm intervals in the 290−420 nm region by using dye laser photolysis coupled with cavity ring-down spectroscopy. Absorption cross sections of glyoxal have been measured. The HCO radical is its photodissociation product. The dependence of the HCO quantum yield on photodissociation wavelength, glyoxal pressure, and nitrogen buffer gas pressure has been determined. The HCO yields decrease with increasing glyoxal pressure in the 1−8 Torr range, owing to the increasing HCO radical reactions at higher glyoxal pressures and quenching by ground-state glyoxal. After separation of the contribution of HCO radical reactions, the aldehyde pressure quenching effect was still observed in the 320−420 nm region, and this effect increased with increasing wavelength. The HCO radical yields (all λ) and the ratios of quenching to unimolecular decay rate constants of excited glyoxal ($\lambda \geq 320$ nm) are given. The peak HCO yield is 2.01 ± 0.08 (error quoted only includes 1σ measurement uncertainty) at 390 nm, consistent with the occurrence of the $(HCO)_2 + h\nu \rightarrow 2HCO$ channel. The HCO radical yields are around 1.56 ± 0.22 in the 320−370 nm region, indicating the simultaneous occurrence of $(HCO)_2 + h\nu \rightarrow 2HCO$ and $(HCO)_2 + h\nu \rightarrow HCO + H + CO$ channels. The HCO radical yields are 0.50 ± 0.01, 0.68 ± 0.02, and 0.84 ± 0.07 at 290, 300, and 310 nm, respectively, which may suggest the opening of an additional photolysis channel at higher photon energies. The dependence of the HCO quantum yield on nitrogen buffer gas pressure was examined between 10 and 400 Torr. The HCO radical yields are independent of nitrogen pressure in the 290−370 nm range, but they decrease with increasing nitrogen pressure in the 380−420 nm region. A comparison of the wavelength-dependent HCO radical yields with results obtained from previous dynamics and quenching studies provides insight into the mechanism of glyoxal photodissociation as a function of wavelength.

Introduction

Glyoxal, $(CHO)_2$, is formed in the atmosphere by air photooxidation of aromatic hydrocarbons in the presence of NO_x and by ozonolysis and OH-initiated oxidation of 1,3-butadiene.[1−3] The electronic absorption spectrum of glyoxal consists of two bands in the 220−480 nm region.[4,5] The higher-energy band (220−320 nm) is entirely diffuse and peaks at 280 nm, while the longer-wavelength band (340−480 nm) exhibits fine structure with maximum absorption at 455 nm. The longer-wavelength band is composed of two transitions, an extremely weak $\tilde{a}\ ^3A_u \leftarrow \tilde{X}\ ^1A_g(\pi^*\leftarrow n)$ transition with a 520.8 nm 0−0 band and a relatively much stronger $\tilde{A}\ ^1A_u \leftarrow \tilde{X}\ ^1A_g(\pi^*\leftarrow n)$ transition with a 455 nm 0−0 band. Absorption cross sections of glyoxal in the actinic UV region have been measured,[6−8] and there is a good agreement between cross section values reported by Orlando and Tyndall[7] and by Horowitz and co-workers.[8] Photodissociation of glyoxal has been investigated in an environmental chamber by Plum and co-workers.[6] Their study indicated that photolysis is the major tropospheric loss process for glyoxal. However, the effective glyoxal photolysis quantum yield reported depends on the spectral distribution used in their study. There is also a recent paper[9] that reports the photolysis frequency of glyoxal relative to NO_2. The following dissociation pathways are thermodynamically allowed, following excitation of glyoxal in the near UV and visible region:

$$(HCO)_2 + h\nu \rightarrow 2HCO\ (\lambda \leq 417\ \text{nm}) \quad (1)$$

$$\rightarrow H + CO + HCO\ (\lambda \leq 334\ \text{nm}) \quad (2)$$

$$\rightarrow CH_2O + CO\ (\text{all}\ \lambda) \quad (3)$$

$$\rightarrow H_2 + 2CO\ (\text{all}\ \lambda) \quad (4)$$

$$\rightarrow CO + HCOH\ (\lambda \leq 546\ \text{nm}) \quad (5)$$

where threshold wavelengths were calculated from the corresponding enthalpy changes. The collisionless photodissociation dynamics of glyoxal in the 440−455 nm region have been investigated extensively[10−13] and the occurrence of the $CH_2O + CO$, $H_2 + 2CO$, and $CO + HCOH$ photolysis pathways have been confirmed (glyoxal photolysis pathways leading to the formation of $CH_2O + CO$, $H_2 + 2CO$, and $CO + HCOH$ are referred to as the formaldehyde channel, the triple whammy channel, and the hydroxymethylene channel in the literature[12,14]). Parmenter's group observed formaldehyde and carbon monoxide products following collision-free dissociation of glyoxal at 455 nm which suggested the occurrence of dissociation via internal conversion to the ground singlet electronic surface ($\tilde{X}\ ^1A_g$) before the formation of products.[10] Burak and co-workers used vacuum UV laser-induced fluorescence to monitor the internal state distribution and vector correlation of the CO product following selective excitation (440−455 nm) of glyoxal to

* To whom correspondence should be addressed. E-mail: zhul@orkney.ph.albany.edu. Telephone: (518) 474-6846. Fax: (518) 473-2895.

10.1021/jp022440d CCC: $25.00
Published on Web 05/23/2003

individual vibronic levels of its first excited singlet state ($\tilde{A}\ ^1A_u$).[11] There is a molecular beam study of the photodissociation of glyoxal at 440 nm in which the arrival time distribution of mass 28 and 30 fragments has been examined.[12] This molecular beam work suggested that dissociation channels $H_2CO + CO$, $H_2 + 2CO$, and $HCOH + CO$ coexist at 440 nm, with relative yields of 65%, 28%, and 7%, respectively. H_2 production has been detected following excitation of glyoxal at 440 nm using vacuum UV laser-induced fluorescence and $(2 + 1)$ resonance enhanced multiphoton ionization, and the internal state distribution of H_2 has been measured.[13] Fluorescence spectra ($\tilde{A}\ ^1A_u \rightarrow \tilde{X}\ ^1A_g$ transition) of glyoxal in a supersonic jet following laser excitation in the 393−417 nm region[14] have been recorded. Chang and Chen[15] observed quantum beats resulting from the coherently excited mixed triplet and singlet states in the decay of fluorescence from jet-cooled glyoxal. They also proposed a dissociation channel, e.g., formation of 2HCO, from glyoxal photolysis at the excited triplet surface in addition to the $CH_2O + CO$, $H_2 + 2CO$, and $CO + HCOH$ product channels resulting from dissociation at the ground singlet surface. In the presence of collisional perturbation, intersystem crossing to the triplet state ($^1A_u - {}^3A_u$) readily occurs,[16] and the following glyoxal photolysis studies were obtained under bulk conditions. Langford and Moore measured the HCO radical yield from photodecomposition of glyoxal at 308 nm by using laser photolysis/resonance absorption technique.[17] Our group previously used cavity ring-down spectroscopy to quantify the HCO radical yields from the photodissociation of glyoxal at 193, 248, 308, and 351 nm.[18] Determination of wavelength-dependent photolysis pathways and quantum yields of glyoxal in the actinic UV region allows an elucidation of its atmospheric fates and provides insight into the mechanism of glyoxal photodissociation as a function of wavelength.

Presented in this paper are results obtained from an experimental investigation of the photolysis of glyoxal at 10 nm intervals in the 290−420 nm region, using dye laser photolysis combined with cavity ring-down spectroscopy.[19,20] Absorption cross sections of glyoxal have been obtained at each of the wavelengths studied. The formation yields of HCO, and their dependence on photolysis wavelength, glyoxal pressure, and total pressure, have been determined. Absolute HCO radical concentrations were calibrated relative to those obtained from formaldehyde photolysis or from the $Cl + H_2CO \rightarrow HCl + HCO$ reaction. Atmospheric photodissociation rate constants and lifetimes of glyoxal have been estimated as a function of zenith angle for cloudless conditions at sea level and at 760 Torr nitrogen pressure.

Experimental Technique

The experimental apparatus has been described in detail in our previous publications.[21−24] Two laser systems, one for the photolysis of glyoxal and the other for the detection of HCO photoproduct, were used in the experiments. Photolysis radiation was provided either by the fundamental or by the second-harmonic output of a tunable dye laser pumped by a 308 nm XeCl excimer laser (~200 mJ/pulse). Laser dyes used to cover the 290−330 nm region included Rhodamine 6G, Rhodamine B, Rhodamine 101, and DCM. Laser dyes used in the 340−420 nm region were *p*-terphenyl, DMQ, QUI, and Stilbene 3. The photolysis beam was introduced into the reaction cell at a 15° angle with the main cell axis through a sidearm. The monitoring laser pulse (613−617 nm) from a dye laser pumped by a nitrogen laser was directed along the main optical axis of the cell. The pump and probe laser beams crossed one another at the center of the reaction cell, vacuum-sealed with a pair of high-reflectance cavity mirrors. The base path length between the two cavity mirrors was 50 cm. A fraction of the probe laser pulse was injected into the cavity through the front mirror. The light intensity decay inside the cavity was measured by monitoring the weak transmission of light through the rear mirror with a photomultiplier tube (PMT). The PMT output was amplified, digitized, and sent to a computer. The decay curve was fitted to a single-exponential decay function, from which the ring-down time constant and the total loss per optical pass were computed. The ring-down time constant was on the order of 27 μs for an empty cavity, with 60 ppm transmission loss per mirror. In the presence of absorbing species, the cavity decay time shortened. By measurement of the cavity losses with and without a photolysis pulse, the HCO absorption from the photolysis of glyoxal was obtained. A pulse/delay generator was used to vary the delay time between the firing of the photodissociation and the probe lasers. The photolysis laser pulse energy was measured with a calibrated Joulemeter.

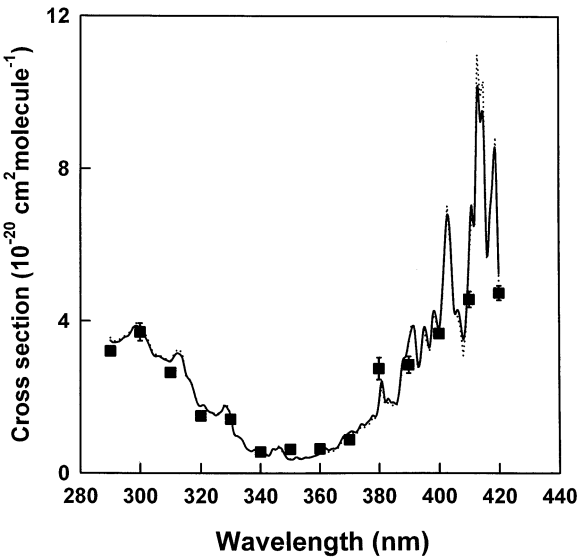

Figure 1. Absorption cross sections of glyoxal in the 290−420 nm region: (■) this work; (−) Orlando and Tyndall;[7] (...) Horowitz et al.[8]

Gas pressure was measured at the center of the reaction cell with a Baratron capacitance manometer. Quantum yield measurements were made at a laser repetition rate of 0.1 Hz to ensure replenishment of gas samples between successive laser pulses. Spectrum scan was performed at a laser repetition rate of 1 Hz. All experiments were carried out at an ambient temperature of 293 ± 2 K.

Glyoxal was produced by pyrolyzing the glyoxal trimeric dihydrate (≥99%; Aldrich) in the presence of phosphorus pentoxide (P_2O_5) in a vacuum manifold.[25] The gas-phase sample was collected in a glass bulb after passing through a P_2O_5 column. Formaldehyde was generated by pyrolysis of polymer paraformaldehyde (≥95% purity; Aldrich) at 110 °C. Nitrogen (≥99.999% purity; Northeast Gas Technology) and chlorine (≥99.5% purity; Matheson) were used without further purification.

Results and Discussion

Absorption Cross Sections of Glyoxal in the 290—420 nm Region. Shown in Figure 1 and Table 1 are the room-temperature absorption cross sections of glyoxal determined at 10 nm intervals in the 290−420 nm region. The absorption cross

TABLE 1: Absorption Cross Sections of Glyoxal as a Function of Wavelength

λ (nm)	σ (10^{-20} cm^2 molecule^{-1})
290	3.21 ± 0.07[a]
300	3.71 ± 0.23
310	2.65 ± 0.01
320	1.51 ± 0.12
330	1.42 ± 0.06
340	0.56 ± 0.01
350	0.63 ± 0.03
360	0.64 ± 0.07
370	0.88 ± 0.04
380	2.75 ± 0.29
390	2.85 ± 0.22
400	3.67 ± 0.05
410	4.57 ± 0.21
420	4.74 ± 0.19

[a] Uncertainty (1σ) represents experimental scatter.

section at each wavelength was obtained by monitoring the transmitted photolysis photon intensity as a function of glyoxal pressure in the cell, and by applying Beer's law to the data obtained. Error bars quoted (1σ) are the estimated precision of cross section determination, which includes the standard deviation for each measurement (~0.5%) plus the standard deviation about the mean of at least four repeated experimental runs. Besides random errors, systematic errors also contribute to the uncertainty in cross section values. The major sources of systematic errors are those involving pressure (0.1%) and path length (0.2%) determinations and those resulting from the presence of impurity (~1%) in glyoxal. When relative (see Table 1) and systematic errors are summed, the overall uncertainty for glyoxal cross section measurements is about 5−10% for all wavelengths. Included in Figure 1 for comparison are cross section results reported by Orlando and Tyndall[7] and by Horowitz and co-workers.[8] Our cross section data for glyoxal agree to within 10% with those obtained previously in the 290−310 nm region and at 330, 340, 400, and 420 nm, 15% at 320, 370, and 390 nm, 20% at 360 and 410 nm, 35% at 380 nm, and 45% at 350 nm. The difference between our cross section value at 380 nm and those obtained previously may be the result of a difference in spectral resolution used in various studies. The difference between our cross section data and those obtained previously at 350 nm is probably a result of its low cross section value, and thus it is subject to higher uncertainty.

Time-Resolved Studies of the Photolysis of Glyoxal in the 290—420 nm Region. Displayed in Figure 2 is a cavity ring-down absorption spectrum of the product after 390 nm photolysis of glyoxal. Also shown in the same figure is a previously reported absorption spectrum of HCO in the same wavelength region.[26] A comparison of these two spectra indicates that the HCO radical is a photolysis product of glyoxal. The cavity ring-down spectrometer was tuned to the HCO X^2A'' (0,0,0) → A^2A' (0,9,0) R bandhead at 613.8 nm, and the HCO concentration was followed as a function of time. Figure 3 shows a time-dependent variation of the HCO concentration obtained in the 390 nm photolysis of 3 Torr of glyoxal, along with a fit of the HCO decay profile using the following kinetic scheme:

$$HCO + HCO \rightarrow H_2CO + CO \quad (6)$$

$$HCO + (HCO)_2 \rightarrow \text{products} \quad (7)$$

This modeling scheme assumes that the $(HCO)_2 + h\nu \rightarrow 2HCO$ channel is the only important radical formation channel from the photolysis of glyoxal at 390 nm. (As described in a later

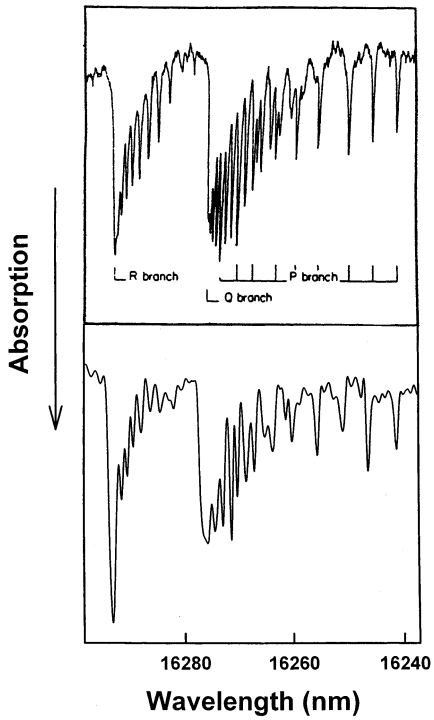

Figure 2. Lower trace: low-resolution cavity ring-down absorption spectrum of the product from 390 nm photolysis of 6.2 Torr of glyoxal. Upper trace: intracavity laser absorption spectrum of the (000) → (090) vibronic transition of HCO following photolysis of 0.1 Torr of CH_3-CHO/10 Torr Ar at 266 nm (adapted from ref 26).

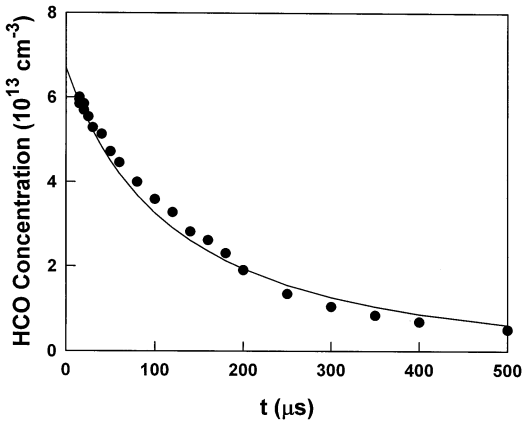

Figure 3. Time-dependent variation of the HCO radical concentration in the photolysis of 3 Torr of glyoxal at 390 nm. Filled circles: experimental results. Solid line: calculated profile using the ACUCHEM simulation program.

section, the HCO yield from the photodissociation of glyoxal at 390 nm is 2.01.) At the detection time ($t \geq 15$ μs) and glyoxal pressure (3−6 Torr) used, the rotational and the vibrational relaxation of the HCO fragment from glyoxal photolysis is expected to be completed (single collision occurs at ~0.03 μs for 3 Torr of glyoxal at room temperature). Time-resolved HCO decay profiles from the photodissociation of 3 and 6 Torr glyoxal were compared with those calculated by the ACUCHEM simulation program.[27] The following input parameters were used: rate constants for the HCO + HCO and HCO+$(HCO)_2$ reactions ($k_{HCO+HCO}$ and $k_{HCO+(HCO)_2}$), and the initial HCO concentration ($[HCO]_0$). Initial values of $k_{HCO+HCO}$ and $k_{HCO+(HCO)_2}$ were given to the program, and the simulated HCO profiles were compared with the experimental results. Values of $k_{HCO+HCO}$ and $k_{HCO+(HCO)_2}$ were adjusted until optimum fits

of experimental profiles were accomplished. Coefficients $k_{HCO+HCO}$ and $k_{HCO+(HCO)_2}$ thus extracted are $(4.7 \pm 0.6) \times 10^{-11}$ and $(2.9 \pm 0.4) \times 10^{-14}$ cm^3 molecule^{-1} s^{-1}, respectively, where uncertainty (1σ) represents experimental scatter only. The HCO decay profiles at these two glyoxal pressures are well fitted by the extracted $k_{HCO+HCO}$ and $k_{HCO+(HCO)_2}$. The accuracy of the $k_{HCO+HCO}$ measurement is affected by the accuracy in the determination of the HCO absorption cross section (σ_{HCO}) and its initial concentration ($[HCO]_0$) and by the time resolution of the cavity ring-down spectroscopy ($\sim$15$-$24 μs around 613 nm). The σ_{HCO} value used in the calculation was $\sim 1.8 \times 10^{-18}$ cm^2/molecule. The initial HCO concentration was in the range of 6.7×10^{13} to 10.3×10^{13} molecules·cm^{-3} when the glyoxal pressure was varied between 3 and 6 Torr. The overall uncertainty in the extracted value of $k_{HCO+HCO}$ is about 50%. The extracted $k_{HCO+HCO}$ agrees well with the recommended rate constant[28] for the HCO + HCO reaction ($k = 2.5 \times 10^{-11}$ to 10.0×10^{-11} cm^3 molecule^{-1} s^{-1} at 300 K). The value of $k_{HCO+(HCO)_2}$ influences mainly the HCO decay profile at a time scale on the order of hundreds of microseconds. Since the HCO decay profiles were measured at glyoxal pressures under the condition $[HCO]_0 \ll [(HCO)_2]_0$, the overall uncertainty in the $k_{HCO+(HCO)_2}$ value is about $\sim$20%.

HCO Quantum Yields from the Photolysis of Glyoxal in the 290$-$420 nm Region. The HCO quantum yields from the photolysis of glyoxal were determined from the ratio of the HCO concentration produced in the photolysis/probe laser overlapping region to the absorbed photon density in the same region. The overlapping region could be envisaged as a rectangular solid with width and height defined by the dimensions of the photolysis beam, and length defined by (beam width) $\times$ tan $(15°)^{-1}$, where 15° is the angle ($\leq \pm 0.5°$ uncertainty in angle measurement) between the photolysis and probe beams (since the concave cavity mirrors have 6 m radii of curvature, the probe laser is expected to have a near constant radius in the cavity and the focusing effects of the ring-down cavity mirrors can be neglected). The photolysis beam widths varied between 1.0 and 2.5 mm, depending on the identity of the laser dyes used, while the uncertainty in the beam width measurement is $\sim$15%. Thus, the length of the photolysis/probe laser overlapping region is between 3.7 ± 0.6 and 9.3 ± 1.4 mm. The photolysis beam is absorbed by glyoxal over the entire level arm through which it travels. Absorbed photolysis photon density in the pump/probe laser overlapping region can be calculated from the difference in the transmitted photolysis beam energy entering (E_{in}) and leaving (E_{out}) that region, the individual photon energy (hc/λ) at the photolysis wavelength (λ), and the volume (v) of the overlapping region by using the following formulas:

$$\text{absorbed photon density} = \frac{E_{in} - E_{out}}{h(c/\lambda)v}$$

$$v = \text{beam width} \times \text{beam height} \times \text{length of the overlapping region}$$

The photolysis beam energy entering or leaving the photolysis/probe laser overlapping region can be computed form the incident photolysis beam energy in the cell (E_0), the aldehyde absorption cross section (σ), and its density (n) in the cell, and the absorbing path length by using Beer's law:

$$E_{in} = E_0 \exp(-\sigma n l_1)$$

$$E_{out} = E_0 \exp(-\sigma n l_2)$$

where l_1 is the distance between the photolysis beam entrance and the beginning of the pump/probe laser overlapping region. l_2 is the distance between the photolysis beam entrance and the end of the pump/probe laser overlapping region. The incident photolysis beam energy was measured by a calibrated Joulemeter placed in front of the cell. The incident beam energy inside the cell front window was corrected for transmission loss at the front cell window ($\sim$8% correction) and for reflection of the photolysis beam from the rear cell window (4$-$9% correction). The HCO concentration after the photolysis was acquired by measuring its absorption at 613.80 nm at a photolysis and probe laser delay of 15 μs. To convert HCO absorption into absolute concentration, the absorption cross section of HCO at the probe laser wavelength was determined relative either to the formaldehyde photolysis reaction $H_2CO + h\nu \rightarrow HCO + H$, for which the HCO quantum yield is known,[28] or else to the Cl + $H_2CO \rightarrow$ HCl + HCO reaction. In the 290$-$330 nm region, formaldehyde photolysis calibration was used. H_2CO was produced immediately prior to each calibration run in a glass bulb. The purity of H_2CO was estimated through comparison of its absorption cross sections with literature values.[29] The H_2CO absorption cross section was determined by measuring the transmitted photolysis photon fluence as a function of H_2CO pressure in the cell, and by applying Beer's law to the data obtained. Our H_2CO cross sections (tabulated in Table 2) agree with those obtained by Meller and Moortgat[29] to within 5% at 300 nm, 10% at 290 and 320 nm, 15% at 330 nm, and 50% at 310 nm. The difference in the H_2CO cross section at 310 nm is due mostly to the different spectral resolution used between the present (0.15 cm^{-1} or 0.0014 nm at a photolysis wavelength of 310 nm) and the previous study (0.5 nm) and the fine absorption feature of H_2CO around 310 nm. Although formaldehyde displays some structures in its UV absorption band, we have no difficulty in obtaining reproducible cross section measurements at all wavelengths except for 310 nm. At 310 nm, there is day-to-day fluctuation of cross section values due to the combination of sharp absorption features of formaldehyde at this wavelength and the photolysis laser bandwidth to be larger than formaldehyde line width (the same grading setting was used in H_2CO cross section and HCO yield measurement, and we obtained reproducible HCO radical yield at 310 nm). Since the HCO absorption was measured at 15 μs after the photolysis of H_2CO, the following sequence of reactions has been used to calculate the HCO concentration at $t = 15$ μs (the HCO concentration at $t = 0$ was calculated from the absorbed photon

TABLE 2: Absorption Cross Sections of Formaldehyde and Chlorine

λ (nm)	σ_{H_2CO} (10^{-20} cm^2 molecule^{-1})	σ_{Cl_2} (10^{-20} cm^2 molecule^{-1})
290	1.24 ± 0.14[a]	
300	1.01 ± 0.06	
310	3.34 ± 0.08	
320	1.08 ± 0.10	22.4 ± 0.7
330	4.41 ± 0.15	
340		21.9 ± 0.8
350		20.5 ± 1.8
360		10.5 ± 0.1
370		7.9 ± 0.1
380		3.6 ± 0.3
390		3.3 ± 0.1
400		1.8 ± 0.1
410		1.1 ± 0.1
420		0.99 ± 0.12

[a] Uncertainty (1σ) represents experimental scatter.

density in the photolysis/probe laser overlapping region and the literature[28] HCO yields from the H_2CO photolysis):

$$HCO + HCO \rightarrow H_2CO + CO \quad (6)$$

$$H + HCO \rightarrow H_2 + CO \quad (8)$$

$$H + H_2CO \rightarrow H_2 + HCO \quad (9)$$

A $k_{HCO+HCO}$ of 4.7×10^{-11} cm^3 molecule^{-1} s^{-1} determined from this work was used in the fitting. Literature $k_{H + HCO} = 1.5 \times 10^{-10}$ cm^3 molecule^{-1} s^{-1} and $k_{H + H2CO} = 3.8 \times 10^{-14}$ cm^3 molecule^{-1} s^{-1} were also used in the simulation.[30] At 320 nm and in the 340−420 nm region, the absolute HCO concentration was calibrated relative to the $Cl + H_2CO$ reaction. The $Cl + H_2CO$ calibration was made by first introducing only H_2CO into the cell and measuring the HCO radical absorption from the formaldehyde photolysis. Initial concentrations of HCO radicals ($[HCO]_0$) and hydrogen atoms ($[H]_0$) from formaldehyde photolysis were computed. A mixture of chlorine (Cl_2) and H_2CO (an equal amount of H_2CO as in the formaldehyde photolysis) was subsequently introduced into the cell, and the HCO absorption at 15 μs after the photolysis of a Cl_2/H_2CO mixture was determined. Chlorine and formaldehyde were introduced into the cell at a pressure ratio of $P_{Cl_2}/P_{H_2CO} = 1{:}5$ ($P_{total} = 0.6$ and 1.2 Torr) to ensure that Cl atoms produced from the photolysis of Cl_2 reacted only with H_2CO. Absorption cross sections of Cl_2 were determined at 320 nm and in the 340−420 nm region. They are listed in Table 2. They agree with literature values[31] to within 5% at 320, 400, and 420 nm, 10% at 340, 350, and 370 nm, 15% at 390 and 410 nm, 20% at 360 nm, and 30% at 380 nm. The following sequence of reactions can occur at 15 μs after the photolysis of a Cl_2/H_2CO mixture:

$$Cl + H_2CO \rightarrow HCl + HCO \quad (10)$$

$$Cl_2 + HCO \rightarrow HClCO + Cl^{\ddagger} \quad (11)$$

$$Cl^{\ddagger} + H_2CO \rightarrow HCl^{\ddagger} + HCO \quad (12)$$

$$H + Cl_2 \rightarrow HCl + Cl^* \quad (13)$$

$$Cl^* + H_2CO \rightarrow HCl^* + HCO \quad (14)$$

Chlorine atoms in eq 10 are produced from the photolysis of Cl_2. Those in eq 11 are generated from the reaction of Cl_2 with HCO. Chlorine atoms in eq 13 are a product of the reaction of Cl_2 with H atoms generated from formaldehyde photolysis. Reactions 12 and 14 represent the generation of HCO through reactions of secondary Cl atoms with H_2CO. The following input parameters were given to the ACUCHEM program to calculate the HCO concentration at 15 μs after the photolysis of a Cl_2/H_2CO mixture: the initial concentration of chlorine atoms ($[Cl]_0$) from the photolysis of Cl_2, the initial concentrations of formaldehyde ($[H_2CO]_0$) and chlorine ($[Cl_2]_0$), the initial concentrations of HCO radicals ($[HCO]_0$) and hydrogen atoms ($[H]_0$) from the photolysis of formaldehyde, and the literature rate constants (in units of cm^3 molecule^{-1} s^{-1}) for the $Cl + H_2CO$ (7.3×10^{-11}), $HCO + Cl_2$ (7.6×10^{-12}), and $H + Cl_2$ (2.0×10^{-11}) reactions.[28,32,33] The HCO absorption cross section (σ_{HCO}) was obtained from the equation

$$A_{t=15\,\mu s} = \sigma_{HCO}[HCO]_{t=15\,\mu s}2l$$

where $A_{t=15\,\mu s}$ and $[HCO]_{t=15\,\mu s}$ are, respectively, the round-trip HCO absorption and HCO concentration at 15 μs after the photolysis of a Cl_2/H_2CO mixture while l equals (photolysis beam width)/sin (15°). At 320 nm, both formaldehyde photolysis and the $Cl + H_2CO$ reaction were used to calibrate the absolute HCO concentration. The HCO absorption cross sections obtained by these two methods agree to within 7%.

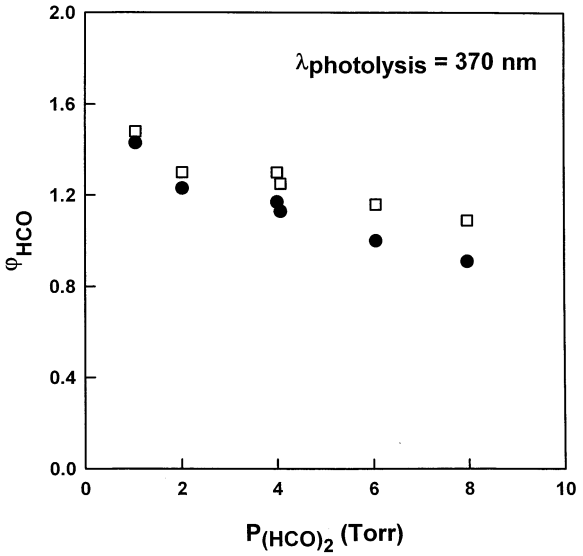

Figure 4. HCO radical quantum yields as a function of glyoxal pressure at a photolysis wavelength of 370 nm. Filled circles: uncorrected yields. Squares: yields that have been corrected for the HCO radical reactions at 15 μs.

The dependence of the HCO radical quantum yields on glyoxal pressure was examined by determining the HCO radical yields from the photolysis of 1, 2, 4, 6, and 8 Torr of glyoxal. The HCO radical yields decrease with increasing glyoxal pressure at all wavelengths, possibly due to the quenching of the excited glyoxal by the ground-state glyoxal molecules and the increasing HCO radical reactions at higher glyoxal pressures. To separate HCO radical reactions from the quenching process, the HCO radical yields at $t = 0$ was deduced by using the ACUCHEM program to convert the experimentally determined HCO radical yields at 15 μs following photolysis to that at $t = 0$. The HCO radical reactions considered in the simulation include the following: $HCO + HCO \rightarrow H_2CO + CO$, $H + HCO \rightarrow H_2 + CO$, and $HCO + (CHO)_2 \rightarrow$ products in the 290−370 nm region; $HCO + HCO \rightarrow H_2CO + CO$ and $HCO + (CHO)_2 \rightarrow$ products in the 380−420 nm region (as described later in this section, the HCO radical yield of ~1.5 at 370 nm seems to suggest the simultaneous occurrence of the $(HCO)_2 + h\nu \rightarrow 2HCO$ and $(HCO)_2 + h\nu \rightarrow HCO + H + CO$ photolysis channels). After separation of the HCO radical reactions, the glyoxal pressure quenching effect was still observed in the 320−420 nm region. Figure 4 shows plots of both the uncorrected and the corrected HCO yields as a function of glyoxal pressure at a photolysis wavelength of 370 nm. As seen from this figure, the corrected HCO quantum yields still decrease with increasing glyoxal pressure at 370 nm, indicating a glyoxal pressure quenching effect. The corrected reciprocal HCO radical yields were plotted against glyoxal concentration ($[(HCO)_2]$) according to the Stern−Volmer equation:

$$1/\varphi_{HCO} = 1/\varphi^0_{HCO} + (k^Q_{(HCO)_2}/k^D_{(HCO)_2})[(HCO)_2]$$

where φ^0_{HCO} is the HCO yield extrapolated to zero glyoxal pressure, and $k^Q_{(HCO)_2}/k^D_{(HCO)_2}$ is the ratio of quenching to unimolecular decay rate constant of excited glyoxal. Displayed in Figure 5 is a plot of $1/\varphi_{HCO}$ vs $[(HCO)_2]$ obtained from 370

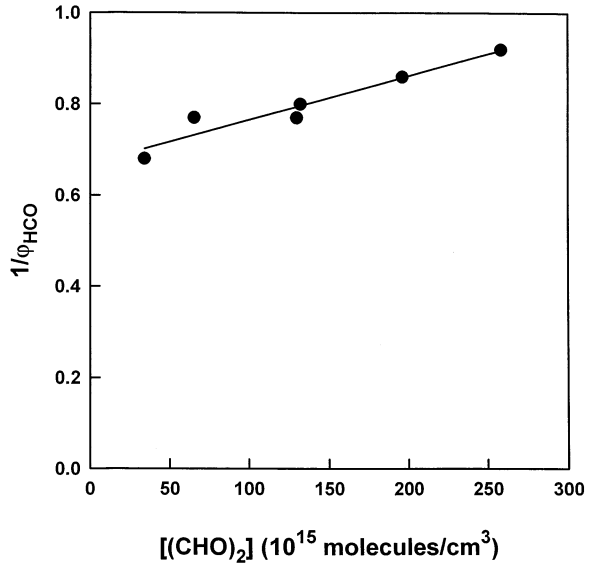

Figure 5. Stern−Volmer plot of the reciprocal HCO radical yields as a function of $(HCO)_2$ concentration at a photolysis wavelength of 370 nm. Filled circles: experimental data. Solid line: fit of the data to the Stern−Volmer expression.

TABLE 3: Values of φ^0_{HCO} and k^Q/k^D from the Photolysis of Glyoxal

λ (nm)	φ^0_{HCO}	k^Q/k^D (10^{-18} cm^3/molecule)
290	0.50 ± 0.01[a]	0
300	0.68 ± 0.02	0
310	0.84 ± 0.07	0
320	1.43 ± 0.02	0.49 ± 0.06
330	1.77 ± 0.12	0.46 ± 0.28
340	1.54 ± 0.01	0.62 ± 0.03
350	1.34 ± 0.06	0.37 ± 0.20
360	1.62 ± 0.15	0.71 ± 0.22
370	1.49 ± 0.04	0.96 ± 0.15
380	1.91 ± 0.13	0.77 ± 0.28
390	2.01 ± 0.08	1.0 ± 0.1
400	0.74 ± 0.08	1.1 ± 0.2
410	0.56 ± 0.04	1.6 ± 0.9
420	0.48 ± 0.03	2.0 ± 0.1

[a] See text for the discussion of true errors.

nm photolysis of $(HCO)_2$. As can be seen, the plot is linear. Values of φ^0_{HCO} (all λ) and $k^Q_{(HCO)_2}/k^D_{(HCO)_2}$ ($\lambda \geq 320$ nm) as a function of the photolysis wavelength are tabulated in Table 3 and plotted in Figure 6 (φ^0_{HCO} only). As seen from Figure 6, the peak HCO yield is 2.01 ± 0.08 (1σ uncertainty) at 390 nm, consistent with the occurrence of the $(HCO)_2 + h\nu \rightarrow 2HCO$ channel. The HCO radical yields are on the order of 1.56 ± 0.22 in the 320−370 nm region, indicating the simultaneous occurrence of the $(HCO)_2 + h\nu \rightarrow 2HCO$ and $(HCO)_2 + h\nu \rightarrow HCO + H + CO$ channels with branching ratios for these two channels of ∼0.56 and ∼0.44, respectively. Although the calculated photochemical threshold for the opening of HCO + H + CO channel from glyoxal photolysis is 334 nm, the HCO yield of ∼1.5 at 370 nm seems to suggest the occurrence of this channel at wavelengths longer than the calculated photochemical threshold. One possible explanation for the occurrence of HCO + H + CO product channel at photolysis wavelength longer than the calculated photochemical threshold is that there is probably uncertainty in the enthalpy of formation of HCO. We observed a similar effect in the benzaldehyde photolysis.[34] Although the calculated photochemical threshold for the formation of HCO + C_6H_5 is 292 nm, we observed HCO product at photolysis wavelength of 308 nm. Another possible explanation is that the thermalized glyoxal molecules might contribute their

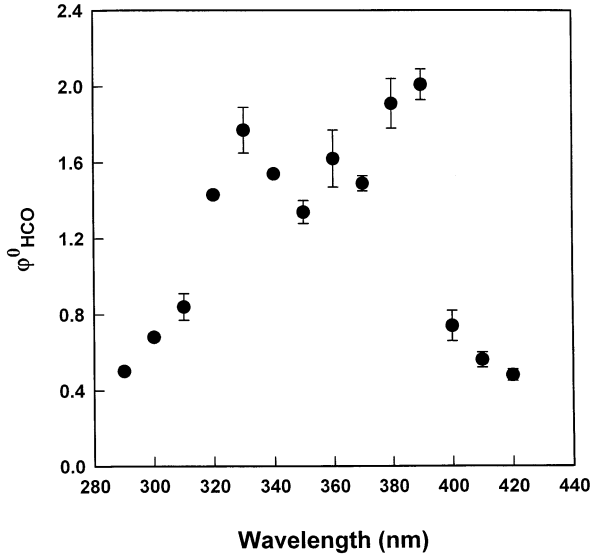

Figure 6. Zero-pressure HCO radical yields from glyoxal photolysis as a function of photodissociation wavelength.

internal energy to reach the photodissociation threshold. The HCO radical yields from glyoxal photolysis are 0.50 ± 0.01, 0.68 ± 0.02, and 0.84 ± 0.07 at 290, 300, and 310 nm, respectively, which may be suggestive of the opening of an additional photolysis pathway at higher photon energies. The reduced HCO yields at $\lambda \geq 400$ nm may be the result of dissociation at near-threshold wavelengths, and/or the result of the opening of competing dissociative processes such as the opening of $CH_2O + CO$, $H_2 + 2CO$, and CO + HCOH product channels at the longer-wavelength tail. Error bars in quantum yield measurements were calculated using cumulative error analysis of the standard deviations of at least two $1/\varphi_{HCO}$ vs $[(HCO)_2]$ plots. Systematic errors include uncertainties in the determination of the following parameters: HCO absorption cross section (∼20%), glyoxal concentration and cross section (10−15%), pulse energy (∼5%), angle between the photolysis and probe lasers (3%), and the dye laser width. Since the HCO radical yields from the photolysis of glyoxal were determined relative to those obtained from H_2CO photolysis or from the $Cl + H_2CO$ reaction, uncertainty in dye laser width measurement should not directly affect the relative HCO quantum yields, but it will affect the correction of the HCO radical reactions. As a result, uncertainty in dye laser width measurement will indirectly affect the yield data. Taken together the relative (∼10%) and systematic errors, the overall uncertainty in the determination of φ^0_{HCO} is about 50% in the wavelength range studied. Values of $k^Q_{(HCO)_2}/k^D_{(HCO)_2}$ ($\lambda \geq 320$ nm) determined in this work are in the range of 0.37×10^{-18} to 2.0×10^{-18} cm^3/molecule. The previously reported quenching rate constant[35] for low-lying levels of the ^1A_u state of glyoxal by ground-state glyoxal molecule is around 6.3×10^{-11} cm^3 s^{-1}. Thus, unimolecular decay rate constants of excited glyoxal in the presence of excess ground-state glyoxal molecules are on the order of 1.7×10^8 to 3.2×10^7 molecule s^{-1}.

A comparison of the wavelength-dependent HCO radical yields from glyoxal photolysis obtained from this work with results[15,36] obtained from the previous glyoxal fluorescence spectra and lifetime measurements sheds light on the mechanism of glyoxal photodissociation. Chang and Chen[15] measured fluorescence spectra of glyoxal in a supersonic jet following laser excitation in the 393−417 nm region and observed quantum beats resulting from the coherently excited mixed triplet and singlet states in the decay of fluorescence. They

proposed a new dissociation channel, e.g., formation of 2HCO, from glyoxal photolysis at the excited triplet surface. Our HCO radical yields of about 2 at 380 and 390 nm confirm the prediction of the $(HCO)_2 + h\nu \rightarrow 2HCO$ channel by Chang and Chen in the wavelength region they studied. As can be seen from the description follows, intersystem crossing to the excited triplet is very efficient at the excitation energy ($\lambda \leq 390$ nm) and glyoxal pressure (≥ 1 Torr) used. Radical products are most likely a result of dissociation at the excited triplet surface. Van der Werf et al.[36] measured low-pressure glyoxal fluorescence decay time over the $\tilde{A}-\tilde{X}$ absorption band and distinguished three excitation regions as a result of different fluorescence decay behavior. For excitation wavelength at or longer than 420 nm, only a microsecond decay was observed. For excitation wavelength in the 392.5−414.5 nm region, the fluorescence decay showed a short-lived component with lifetime of a few nanoseconds in addition to the long-lived component. For excitation wavelength at or shorter than 392.5 nm, only the nanosecond emission can be observed. Van der Werf et al. interpreted their results in terms of the increasing vibronic singlet−triplet mixing (or increasing triplet-state density) as a function of excess vibrational energy. For excitation wavelength at or longer than 420 nm, the amount of vibronic coupling is almost negligible and the fluorescence decay rate is determined only by zero-order singlet relaxation. For excitation wavelength in the 392.5−414.5 nm region, the decay is determined by both zero-order singlet and zero-order triplet relaxation. The short decay is a result of constructive interference between the molecular eigenstates. For excitation wavelength at or shorter than 392.5 nm, the singlet−triplet mixing is very strong and the molecular eigenstates are essentially pure triplets. The triplet relaxation at high excess energies is efficient through intersystem crossing to the ground state and/or photochemistry. Our HCO radical yields are 0.74 and 0.56 at 400 and 410 nm. At these wavelengths, intersystem crossing to the excited triplet state is not as efficient as that at 390 nm for glyoxal. As a result, both intersystem crossing to the excited triplet and internal conversion to the ground singlet are important. Dissociation can occur at the triplet surface to form radicals ($(HCO)_2 + h\nu \rightarrow 2HCO$) and at the singlet surface to form molecular products (CH_2O + CO, H_2 + 2CO, and CO + HCOH). This explains why the HCO yield increases from 0.56 to 2.0 as the wavelength changes from 410 to 390 nm. Our HCO radical yield is 0.48 at 420 nm. Since our study was carried out in the presence of collision while the previous fluorescence lifetime measurements[36] were conducted in the absence of collision, our results at photolysis wavelength of 420 nm most likely include some contribution from dissociation at excited triplet surface and there is no contradiction between results obtained from our wavelength-dependent HCO yield measurement and the previous fluorescence lifetime measurements. The last statement is supported by the results[37,38] obtained from the investigation of collision-induced intersystem crossing following excitation of glyoxal at 435.8 nm. Anderson and co-workers[37,38] used 435.8 nm radiation from a low-pressure Hg arc to excite glyoxal above the $\tilde{A}\ ^1A_u$ zero-point level. For low pressures of glyoxal (~0.01 Torr), only emission from $\tilde{A}\ ^1A_u$ was observed. At glyoxal pressures above 0.1 Torr, both $\tilde{A}\ ^1A_u$ and $\tilde{a}\ ^3A_u$ emissions were identified.

The dependence of the HCO radical quantum yields on total pressure was examined by maintaining a constant glyoxal pressure and varying the nitrogen buffer gas pressure. The HCO quantum yields were found to be independent of nitrogen buffer gas pressure (10−400 Torr) in the 290−370 nm region, but they decreased with increasing nitrogen pressure in the 380−420 nm region. Figure 7 presents a plot of the reciprocal HCO radical yields from the 390 nm photolysis of glyoxal as a function of nitrogen pressure. The slope of the plot represents the ratio of quenching to the unimolecular decay rate constant of the excited glyoxal by nitrogen $[(k^Q/k^D)_{(CHO)_2,N_2}]$ at 390 nm. Since both $(k^Q/k^D)_{(CHO)_2,N_2}$ and φ^0_{HCO} have been measured as a function of wavelength, the wavelength-dependent HCO radical formation yields from photolysis of glyoxal at 760 Torr nitrogen pressure can be obtained; these are summarized in Table 4. Values of $(k^Q/k^D)_{(CHO)_2,N_2}$ are in the range of 0.055×10^{-18} to 0.21×10^{-18} cm^3/molecule in the 380−420 nm region. The reported quenching rate constant[35] for low-lying levels of the ^1A_u state of glyoxal by nitrogen gas is on the order of 2.2×10^{-11} cm^3 s^{-1}. The unimolecular decay rate constants of excited glyoxal in the presence of excess nitrogen are on the order of 4×10^8 to 1×10^8 molecule s^{-1}.

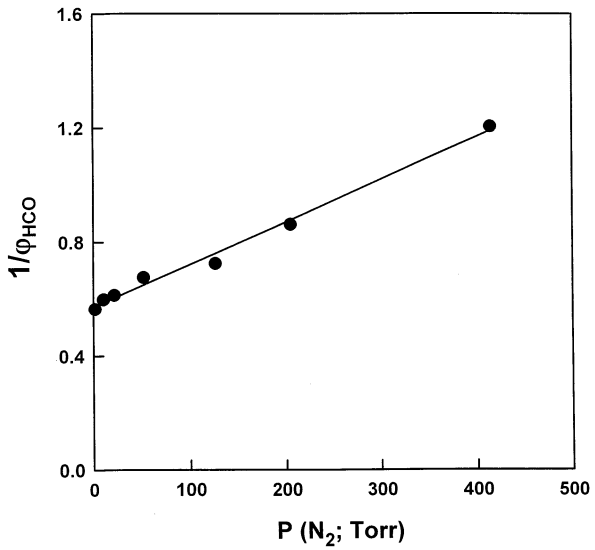

Figure 7. Stern−Volmer plot of the reciprocal HCO yields as a function of nitrogen concentration following 390 nm photolysis of glyoxal. Filled circles: experimental data. Solid line: fit of the data to the Stern−Volmer expression.

TABLE 4: Values of k^Q/k^D and $\varphi_{HCO}^{760\ Torr}$ from the Photolysis of Glyoxal in Nitrogen

λ (nm)	k^Q/k^D (10^{-18} cm^3/molecule)	$\varphi_{HCO}^{760\ Torr}$
380	0.062 ± 0.012[a]	0.49
390	0.055 ± 0.001	0.54
400	0.072 ± 0.012	0.32
410	0.11 ± 0.02	0.22
420	0.21 ± 0.03	0.14

[a] Uncertainty (1σ) represents experimental scatter.

Langford and Moore[17] investigated the photolysis of glyoxal at 308 nm by using laser photolysis/resonance absorption technique. Their experiments suggest that HCO is a direct photoproduct of glyoxal with a quantum yield of 0.8 ± 0.4. Their HCO quantum yield agrees well with the zero-pressure HCO quantum yield of 0.81 at 308 nm obtained from this work. However, Langford and Moore attributed all of the HCO products to having arisen only from the $(CHO)_2 + h\nu$(308 nm) $\rightarrow$ 2HCO channel, based upon the assumption that dissociation into H + CO + HCO was thermoneutral at 308 nm.

Our group[18] previously determined the HCO quantum yields from the photolysis of glyoxal at 193, 248, 308, and 351 nm by using excimer laser photolysis combined with cavity ring-down spectroscopy. HCO quantum yields of 0.69 ± 0.29 and 1.5 ± 0.6 were obtained at 308 and 351 nm, values in good

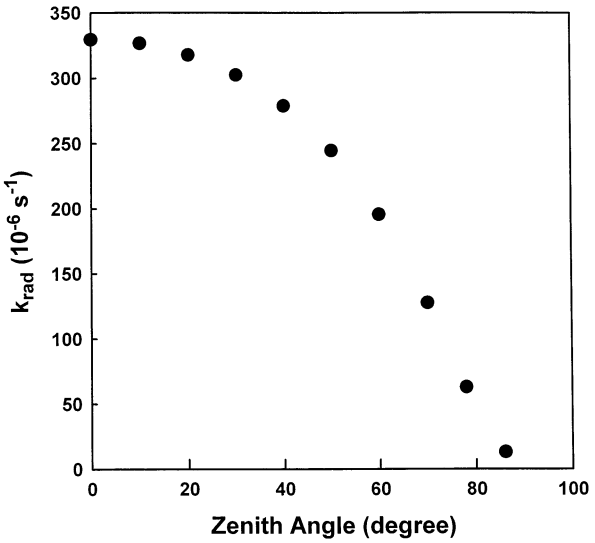

Figure 8. Atmospheric photodissociation rate constants to form radicals from glyoxal photolysis as a function of zenith angle at 760 Torr of nitrogen pressure.

accord with the zero-pressure HCO quantum yields of 0.81 and 1.4 determined from the present work. Consistent with the results from the previous work, there is no nitrogen pressure quenching of HCO quantum yields following photolysis of glyoxal at 308 and 351 nm. There is also no glyoxal presssure quenching effect at 308 nm, again in agreement with results from our previous study. One difference compared with the prior work that merits mention is that we observed in this work a small, but still noticeable glyoxal pressure quenching of the HCO yields following the photolysis of glyoxal at 351 nm.

There have been previous theoretical studies[39,40] that reported transition state geometries, enthalpies of reaction, and activation energies for formation of $H_2CO + CO$, $H_2 + 2CO$, and HCOH + CO products for glyoxal excitation energy in the range of 62.9−65.0 kcal/mol (440−454 nm). Since the previous investigations did not predict the dependence of excitation probabilities into various transition states on photolysis photon energy over 290−420 nm region, a direct comparison with the present experimental results is not possible.

Photodissociation Rate Constants to Form HCO Radicals in the Atmosphere. The atmospheric photodissociation rate constants (k_{rad}) for HCO production (or HO_2 production in the presence of air) from the photolysis of glyoxal were calculated from the actinic solar flux ($J(\lambda)$) reported by Demerjian and co-workers,[41] the absorption cross section of glyoxal ($\sigma(\lambda)$), and the HCO radical yield at 760 Torr nitrogen pressure ($\varphi_{HCO}^{760\ Torr}$) using the relationship

$$k_{rad} = \Sigma\sigma(\lambda)\varphi_{HCO}^{760\ Torr}J(\lambda)\Delta\lambda$$

Radical generation rate constants from the photodissociation of glyoxal were computed as a function of zenith angle under cloudless conditions at sea level and for best-estimate albedo (5% in the 290−400 nm region and 6% in the 400−420 nm region[42]); the results are shown in Figure 8. Our estimated radical formation rate constants from glyoxal photolysis are 3.0×10^{-4} to 2.0×10^{-4} s^{-1} for zenith angles in the 30−60° range. It should be pointed out that the above calculation underestimates the radical formation rates since the oxygen fraction in air is neglected. Oxygen might encourage singlet−triplet mixing of excited glyoxal and thus increase radical formation rates markedly. Assuming a glyoxal photolysis quantum yield of unity in the 290−370 nm region and using a glyoxal photolysis quantum yield of $0.5\varphi_{HCO}^{760\ Torr}$ in the 380−420 nm region determined from this work, its atmospheric photodissociation rate constants are on the order of 2.0×10^{-4} to 1.1×10^{-4} s^{-1} for zenith angles in the 0−60° range. The corresponding photolysis lifetimes are on the order of 1.4−2.4 h. The estimated glyoxal photolysis rate constant is in good agreement with that of $(1.05 \pm 0.30) \times 10^{-4}$ s^{-1} measured directly in the EUPHORE outdoor smog chamber (Valencia) by Moortgat's group.[43] The literature rate constant[6] for OH radical reactions with glyoxal is on the order of 1.2×10^{-11} cm^3 $molecule^{-1}$ s^{-1}, which corresponds to an OH radical reaction lifetime of 24.2 h for a globally averaged OH radical concentration of 10^6 cm^{-3}. Thus, photolysis is a primary removal process for glyoxal in the atmosphere. OH radical reaction is only a minor degradation pathway.

Acknowledgment. We thank Drs. John J. Orlando and Geoffrey S. Tyndall for helpful discussions and for providing us absorption cross section data on glyoxal. We are grateful for the support provided by the National Science Foundation under Grant ATM-0000252.

References and Notes

(1) Liu, X.; Jeffries, H. E.; Sexton, K. G. *Atmos. Environ.* **1999**, *33*, 3005.
(2) Tuazon, E. C.; MacLeod, H.; Atkinson, R.; Carter, W. P. L. *Environ. Sci. Technol.* **1986**, *20*, 383.
(3) Tuazon, E. C.; Atkinson, R.; MacLeod, H.; Biermann, H. W.; Winer, A. M.; Carter, W. P. L.; Pitts, J. N., Jr. *Environ. Sci. Technol.* **1984**, *18*, 981.
(4) Brand, J. C. D. *Trans. Faraday Soc.* **1954**, *50*, 431.
(5) Herzberg, G. *Electronic Spectra and Electronic Structure of Polyatomic Molecules*; Van Nostrand: New York, 1966.
(6) Plum, C. N.; Sanhueza, E.; Atkinson, R.; Carter, W. P. L.; Pitts, J. N., Jr. *Environ. Sci. Technol.* **1983**, *17*, 479.
(7) Orlando, J. J.; Tyndall, G. S. *Int. J. Chem. Kinet.* **2001**, *33*, 149.
(8) Horowitz, A.; Meller, R.; Moortgat, G. K. *J. Photochem. Photobiol. A: Chem.* **2001**, *146*, 19.
(9) Klotz, B.; Graedler, F.; Sørensen, S.; Barnes, I.; Becker, K.-H. *Int. J. Chem. Kinet.* **2001**, *33*, 9.
(10) Loge, G. W.; Parmenter, C. S.; Rordorf, B. F. *Chem. Phys. Lett.* **1980**, *74*, 309.
(11) Burak, I.; Hepburn, J. W.; Sivakumar, N.; Hall, G. E.; Chawla, G.; Houston, P. L. *J. Chem. Phys.* **1987**, *86*, 1258.
(12) Hepburn, J. W.; Buss, R. J.; Butler, L. J.; Lee, Y. T. *J. Phys. Chem.* **1983**, *87*, 3638.
(13) Dobeck, L. M.; Lambert, H. M.; Kong, W.; Pisano, P. J.; Houston, P. L. *J. Phys. Chem.* **1999**, *103*, 10312.
(14) Osamura, Y.; Schaefer, H. F.; Dupuis, M.; Lester, W. A. *J. Chem. Phys.* **1981**, *75*, 5828.
(15) Chang, C.; Chen, I.-C. *J. Chem. Phys.* **2002**, *116*, 2447.
(16) Atkinson, G. H.; Mcllwain, M. E.; Venkatesh, C. G. *J. Chem. Phys.* **1978**, *68*, 726.
(17) Langford, A. O.; Moore, C. B. *J. Chem. Phys.* **1984**, *80*, 4211.
(18) Zhu, L.; Kellis, D.; Ding, C.-F. *Chem. Phys. Lett.* **1996**, *257*, 487.
(19) O'Keefe, A.; Deacon, D. A. G. *Rev. Sci. Instrum.* **1988**, *59*, 2544.
(20) O'Keefe, A.; Scherer, J. J.; Cooksy, A. L.; Sheeks, R.; Heath, J.; Saykally, R. J. *Chem. Phys. Lett.* **1990**, *172*, 214.
(21) Zhu, L.; Johnston, G. *J. Phys. Chem.* **1995**, *99*, 15114.
(22) Cronin, T. J.; Zhu, L. *J. Phys. Chem. A* **1998**, *102*, 10274.
(23) Zhu, L.; Cronin, T.; Narang, A. *J. Phys. Chem. A* **1999**, *103*, 7248.
(24) Chen, Y.; Wang, W.; Zhu, L. *J. Phys. Chem. A* **2000**, *104*, 11126.
(25) Langford, A. O.; Moore, C. B. *J. Chem. Phys.* **1984**, *80*, 4204.
(26) Stoeckel, F.; Schuh, M. D.; Goldstein, N.; Atkinson, G. H. *Chem. Phys.* **1985**, *95*, 135.
(27) Braun, W.; Herron, J. T. *ACUCHEM/ACUPLOT*; computer program for modeling complex reaction systems, National Bureau of Standards: Gaithersburg, MD, 1986.
(28) Atkinson, R.; Baulch, D. L.; Cox, R. A.; Hampson, R. F., Jr.; Kerr, J. A.; Troe, J. *J. Phys. Chem. Ref. Data* **1992**, *21*, 1125.
(29) Meller, R.; Moortgat, G. K. *J. Geophys. Res.* **2000**, *105*, 7089.
(30) Baulch, D. L.; Cobos, C. J.; Cox, R. A.; Esser, C.; Frank, P.; Just, Th.; Kerr, J. A.; Pilling, M. J.; Troe, J.; Walker, R. W.; Warnatz, J. *J. Phys. Chem. Ref. Data* **1992**, *21*, 411.

(31) Maric, D.; Burrows, J. P.; Meller, R.; Moortgat, G. K. *J. Photochem. Photobiol. A: Chem.* **1993**, *70*, 205.
(32) Ninomiya, Y.; Goto, M.; Hashimoto, S.; Kagawa, Y.; Yoshizawa, K.; Kawasaki, M.; Wallington, T. J.; Hurley, M. D. *J. Phys. Chem. A* **2000**, *104*, 7556.
(33) Seeley, J. V.; Jayne, J. T.; Molina, M. J. *Int. J. Chem. Kinet.* **1993**, *25*, 571.
(34) Zhu, L.; Cronin, T. J. *Chem. Phys. Lett.* **2000**, *317*, 227.
(35) Beyer, R. A.; Lineberger, W. C. *J. Chem. Phys.* **1975**, *62*, 4024.
(36) van der Werf, R.; Schutten, E.; Kommandeur, J. *Chem. Phys.* **1975**, *11*, 281.
(37) Anderson, L. G.; Parmenter, C. S.; Poland, H. M.; Rau, J. D. *Chem. Phys. Lett.* **1971**, *8*, 232.
(38) Anderson, L. G.; Parmenter, C. S.; Poland, H. M. *Chem. Phys.* **1973**, *1*, 401.
(39) Koch, D. M.; Khieu, N. H.; Peslherbe, G. H. *J. Phys. Chem. A* **2001**, *105*, 3598.
(40) Li, X.; Schlegel, H. B. *J. Chem. Phys.* **2001**, *114*, 8.
(41) Demerjian, K. L.; Schere, K. L.; Peterson, J. T. *Adv. Environ. Sci. Technol.* **1980**, *10*, 369.
(42) Coulson, K. L.; Reynolds, D. W. *J. Appl. Meteorol.* **1971**, *10*, 1285.
(43) Moortgat, G. K. *Pure Appl. Chem.* **2001**, *73*, 487.